Available online at www.sciencedirect.com

ScienceDirect

Underground Space 4 (2019) 22–30

www.elsevier.com/locate/undsp

Micromechanical study of loading rate effects between a hole and a crack

Shuai Zhou [a], Xiaoying Zhuang [a,b,*]

[a] Institute of Continuum Mechanics, Leibniz University Hannover, Hannover 30167, Germany
[b] Department of Geotechnical Engineering, Tongji University, Shanghai 200092, China

Received 18 March 2018; received in revised form 9 August 2018; accepted 10 August 2018
Available online 15 August 2018

Abstract

The interactions between defects are important in rocks. The micromechanical interactions between a circular hole and a pre-existing crack under uniaxial compression with different loading rates are investigated by the discrete element method (DEM). The crack initiation, crack propagation, and crack coalescence at different loading rates are studied. The loading rates influence the primary as well as secondary cracks. Both the primary and secondary cracks disturb the stress field and displacement field. The DEM simulation explains the initiation position of the primary and secondary cracks. The evolution of the displacement field and the stress field at different loading rates is analyzed. A new displacement field type is observed. The hole is easier to be broken by compression at higher loading rates while it tends to be broken by the coalescence crack at lower loading rates. The high loading rates lead to shielding effects of the hole on the pre-existing crack.

Keywords: Rock; Defect; Loading rate; Cracking processes; DEM; Compressive loading

1 Introduction

The interactions between defects in rocks are important. There are many holes and cracks in rocks. These defects influence the cracking behavior and mechanical properties of rocks. A thorough understanding of the crack initiation, crack propagation, and eventual coalescence processes in rocks is key in the satisfactory characterization and assessment of rock mass. This subsequently benefits geotechnical engineering design and implementation such as the rock slope stability assessment, tunnel support design, shale gas development, and fluid flow prediction in rock masses (Wong & Einstein, 2009a). Owing to the difficulties in direct tensile tests of rock-like materials (Perras & Diederichs, 2014) and the practical application in rock engineering, compressive tests have attracted more research interest. Although related compression tests of specimens containing pre-existing cracks have been conducted (Wong & Einstein, 2009a, 2009b; Lee & Jeon, 2011), the experimental research of specimens containing a crack and a circular void is limited. Experimental (Kranz, 1979) and theoretical (Lee & Ju, 2007) studies regarding the interactions between a crack and a pore have been reported. However, the cracking process was ignored. The specimens containing a hole were studied using uniaxial compression tests (Carter, Lajtai, & Petukhov, 1991), and the influence of pre-existing cracks was neglected. Previous research investigated the interaction between a hole and a pre-existing crack (Zhou, Zhu, Yan, Ju, & Zhang, 2016), while the loading rate effects were not considered. In particular, the influence of loading rate effects on the stress field and displacement field was not investigated in previous research. The strength, fracture toughness, ductility, and degree of fragmentation were increased with the loading

* Corresponding author at: Institute of Continuum Mechanics, Leibniz University Hannover, Hannover 30167, Germany.
E-mail address: zhuang@ikm.uni-hannover.de (X. Zhuang).

https://doi.org/10.1016/j.undsp.2018.08.001

rates (Olsson, 1991; Zhang & Zhao, 2013; Dai, Xia, Zheng, & Wang, 2011; Jackson, Kingman, Whittles, Lowndes, & Reddish, 2008). The mechanical behavior of materials can be studied using DEM (Zhou, Zhu, Ju, Yan, & Chen, 2017; Zhang & Wong, 2013a, 2013b; Ghazvinian, Sarfarazi, Schubert, & Blumel, 2012; Ma, Zhang, Zhang, Yan, & Ye, 2016), molecular dynamics (Zhuang & Zhou, 2018), phase field methods (Badnava, Msekh, Etemadi, & Rabczuk, 2018; Msekh et al., 2017; Areias, Rabczuk, & Msekh, 2016), meshless methods (Zhuang, Zhu, & Augarde, 2014; Zhuang, Cai, & Augarde, 2014; Rabczuk, Areias, & Belytschko, 2007; Rabczuk & Belytschko, 2004; Amiri, Milan, Shen, Rabczuk, & Arroyo, 2014, Amiri, Anitescu, Arroyo, Bordas, & Rabczuk, 2014; Rabczuk, Gracie, Song, & Belytschko, 2010), peridynamics (Ren, Zhuang, & Rabczuk, 2017; Ren, Zhuang, Cai, & Rabczuk, 2016), phantom node method (Chau-Dinh, Zi, Lee, Rabczuk, & Song, 2012; Hamdia, Silani, Zhuang, He, & Rabczuk, 2017), finite element method (Chen et al., 2012; Bek, Hamdia, Rabczuk, & Könke, 2018), as well as other partition-of-unity-based methods (Ghorashi, Valizadeh, Mohammadi, & Rabczuk, 2015; Nguyen-Thanh et al., 2015; Nguyen-Xuan, Liu, Bordas, Natarajan, & Rabczuk, 2013). The particle flow codes (PFC2D and PFC3D) are among the widely used DEM for studying the fracture behavior of rock-like materials. The basic idea is to treat a studied material as an assembly of bonded particles that follow the law of motion (Potyondy & Cundall, 2004; Itasca, 2004). PFC2D has been applied to study the cracking process of rock-like materials containing a single (Zhang & Wong, 2012) and two pre-existing flaw(s) (Zhang & Wong, 2013a) under uniaxial compressive loading. PFC2D has also been used to explore the loading rate effect on the cracking process of flawed specimens under uniaxial compression (Zhang & Wong, 2013b; Xie, Guo, & Xia, 2012). However, the loading rate effect on the stress field and the displacement field of specimens containing a hole and a crack using the DEM has not been studied.

In this work, we study the crack behavior of rock-like materials containing a circular hole and a pre-existing crack at different loading rates. The stress field and displacement field are emphasized. Section 2 summarizes the concept of the DEM. The development of the DEM model and the procedure for the numerical study are detailed in Section 3. The loading rate effect on the stress field of the specimens containing a circular hole and a pre-existing crack is discussed in Section 4 based on the numerical analysis results. Subsequently, the loading rate effect on the displacement field is investigated in Section 5. Finally, Section 6 summarizes the key findings of the present study.

2 Concept of DEM

The continuous material in the DEM is discretized by particles. The macromechanical properties and cracking behavior are determined by the movement of particles. The theoretical details of the DEM have been illustrated previously (Itasca, 2004). The DEM uses the Newton's law of motion to describe the movement of particles

$$F = ma \tag{1}$$

where F, m, and a denote the force, mass, and acceleration of a particle, respectively.

The contact constitutive models at the contact are

$$\boldsymbol{F}^{\mathrm{n}} = \boldsymbol{K}_{\mathrm{h}}^{\mathrm{n}} \boldsymbol{U}^{\mathrm{n}} \tag{2}$$

$$\boldsymbol{F}^{\mathrm{s}} = \boldsymbol{K}_{\mathrm{h}}^{\mathrm{s}} \boldsymbol{U}^{\mathrm{s}} \tag{3}$$

where $\boldsymbol{F}^{\mathrm{n}}$ and $\boldsymbol{F}^{\mathrm{s}}$ denote the normal force component vector and the shear force component vector, respectively. $\boldsymbol{U}^{\mathrm{n}}$ and $\boldsymbol{U}^{\mathrm{s}}$ represent the normal contact displacement component vector and the shear contact displacement component vector, respectively. $\boldsymbol{K}_{\mathrm{h}}^{\mathrm{n}}$ and $\boldsymbol{K}_{\mathrm{h}}^{\mathrm{s}}$ signify the normal stiffness and the shear stiffness at the contact, respectively.

The fracture criteria at the contact are

$$\sigma_{\max} \leqslant \sigma_{\mathrm{c}}^{\mathrm{h}} \tag{4}$$

$$\tau_{\max} \leqslant \tau_{\mathrm{c}}^{\mathrm{h}} \tag{5}$$

where $\sigma_{\max}$ and $\tau_{\max}$ are the maximum tensile stress and the maximum shear stress at the contact, respectively. $\sigma_{\mathrm{c}}^{\mathrm{h}}$ and $\tau_{\mathrm{c}}^{\mathrm{h}}$ denote the normal strength and shear strength at the contact, respectively.

A damping force F_{d} that is added to the contact force is expressed as

$$F_{\mathrm{d}} = -c \times \mathrm{sign}(V) \tag{6}$$

where c is the damping constant, and V is the relative velocity between particles. More details about the DEM can be found in previous literature (Itasca, 2004).

3 Modeling with DEM

In the first step, DEM specimens that are 140 mm high and 70 mm wide, are generated following the procedure described in detail by Itasca (2004). The number of parti-

Table 1
Microscopic parameters used in DEM model.

Parameter	Description	This study
E_{c}	Particle modulus	15 GPa
$\bar{E}_{\mathrm{c}}$	Spring modulus	15 GPa
$k_{\mathrm{n}}/k_{\mathrm{s}}$	Ratio of particle normal to shear stiffness	0.9
$\bar{k}_{\mathrm{n}}/\bar{k}_{\mathrm{s}}$	Ratio of spring normal to shear stiffness	0.9
μ	Contact friction coefficient	0.1
$\bar{\sigma}_{\mathrm{c}}$	Average normal bond strength ± SD	27.4±5.5 MPa
$R_{\max}/R_{\min}$	Ratio of maximum to minimum ball radius	1.66
$\bar{\tau}_{\mathrm{c}}$	Average shear bond strength ± SD	49.7±9.9 MPa
$R_{\min}$	Minimum ball radius	0.25 mm
$\bar{\lambda}$	Bond width multiplier	1.0
ρ	Density	2 378 kg/m^3

cles is close to that in previous research (Zhou et al., 2016; Zhang & Wong, 2012, 2013a, 2013b). The particle radii vary from 0.25 to 0.415 mm, which are chosen to be as small as possible without compromising the computational efficiency and significantly increasing the computation time (Ghazvinian et al., 2012). The parallel bond model is adopted in this study to describe the bond between particles because it can simulate the rock-like material well (Zhou et al., 2016; Zhang & Wong, 2012, 2013a, 2013b).

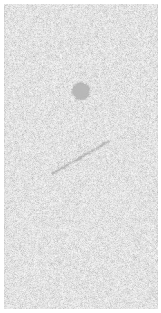

Fig. 1. Schematic diagram of the produced DEM specimen.

The microscopic properties of the particles and the parallel bonds are determined following the default calibration procedure in PFC2D. First, the Young's modulus is matched by setting the material strengths to a large value and varying the particle modulus E_c after a few iterations. Subsequently, the Poisson's ratio, peak strength, crack-initiation stress, and other parameters are matched similarly. More details can be found in previous research (Itasca, 2004). The determined microscopic properties of the particles and the parallel bonds are shown in Table 1 (Zhou et al., 2016).

Specimens containing a circular hole and a pre-existing crack are exhibited in Fig. 1. The diameter of the hole is 8 mm, and the length and thickness of the pre-existing crack are 30 mm and 1 mm, respectively (Zhou et al., 2016). Five loading rates (i.e., 0.01 m/s, 0.08 m/s, 0.2 m/s, 0.6 m/s and 2.0 m/s) from previous work (Xie et al., 2012; Zhang & Wong, 2013b) are chosen in the numerical simulations to investigate the loading rate effects on the cracking behavior. A specimen with a length x and a pre-existing crack inclination angle y is denoted as sx-dy (Zhou et al., 2016). To better investigate the loading rate

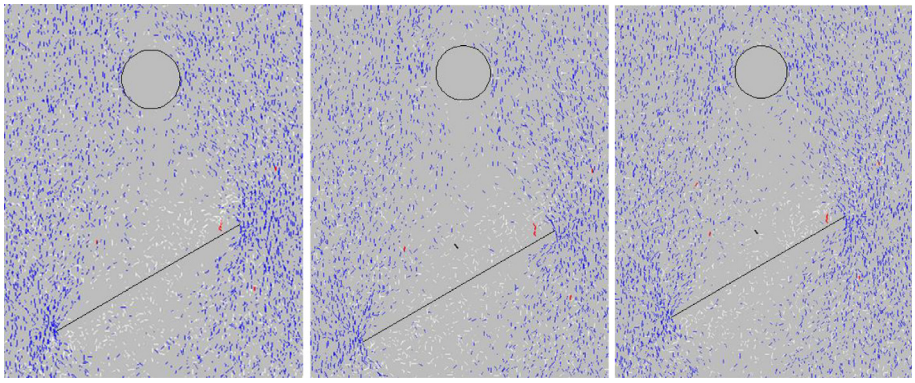

(a) 0.01 m/s (11.4 MPa) (b) 0.08 m/s (11.6 MPa) (c) 0.2 m/s (13.1 MPa)

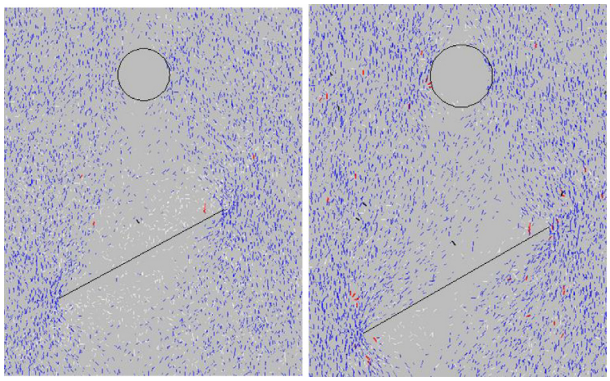

(d) 0.6 m/s (14 MPa) (e) 2.0 m/s (29 MPa)

Fig. 2. Stress field of geometry s30-d30 when the first crack initiates at different loading rates.

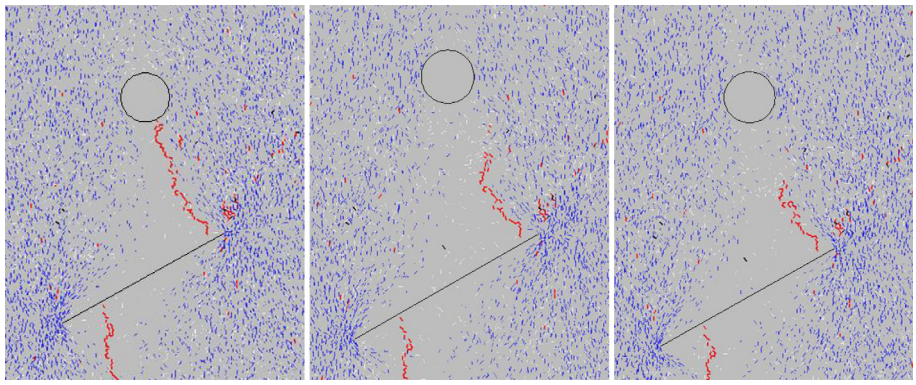

(a) 0.01 m/s (19.4 MPa) (b) 0.08 m/s (20.9 MPa) (c) 0.2 m/s (22.5 MPa)

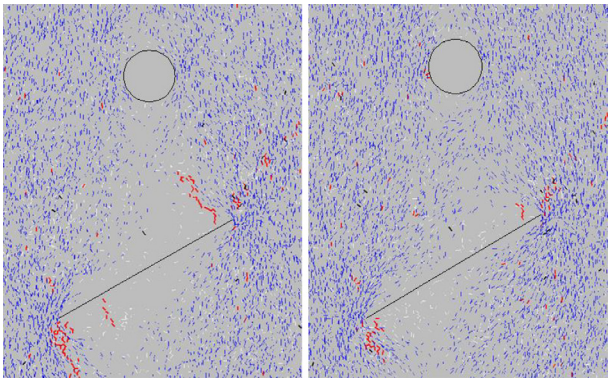

(d) 0.6 m/s (27.8 MPa) (e) 2.0 m/s (29.2 MPa)

Fig. 3. Stress field of geometry s30-d30 when the secondary crack initiates at different loading rates.

effects, the s30-d30 specimen with different loading rates is studied here.

The microtensile crack is represented by a red line and the microshear crack by a black line. A macrocrack is considered formed when three or more microcracks are connected (Zhang & Wong, 2013a). The compressive stress is represented by the blue line, while the tensile stress is signified by the white line in Section 4. The displacement vector is represented by the blue arrow in Section 5.

4 The loading rate effects on the stress field

The cracking processes influence the stress field. The stress field when the first crack initiates at different loading rates is displayed in Fig. 2. The stresses in the parentheses are those corresponding to the specified stages. The dense blue lines in the matrix represent the compressive zone. The white lines around the middle part of the crack, both on the top and the bottom sides, signify the tensile zone. When the loading rate is 0.01 m/s and the axial load is 11.4 MPa in Fig. 2(a), multiple microcracks initiate close to the crack tip, preferentially from the top side of the pre-existing crack. When new cracks initiate from the pre-existing crack, the tensile stress around the pre-existing crack decreases and the newly developed crack tips serve as new stress concentration points. Subsequently, the tensile stress in the upper part of the top surface is partially released. The white lines shift upwards around the newly developed microtensile cracks. Even though some microtensile cracks exist at the lower tip of the pre-existing crack in Fig. 2(e), the stress field around it does not change significantly. This is because these microcracks are disconnected and the middle spaces between these microcracks can carry force. Because the stress intensity degree of the hole is less than that of the crack tip, no microcracks appear around the hole, as shown in Fig. 2 (a)–(e). When the loading rate is 0.08 m/s and the axial load is 11.6 MPa, as shown in Fig. 2(b), the first crack is initiated. The initiation position and the first crack initiation stress are almost the same as that in Fig. 2(a). In other words, the loading rate effect on the first crack when the loading rate is slower than 0.08 m/s is limited, which agrees

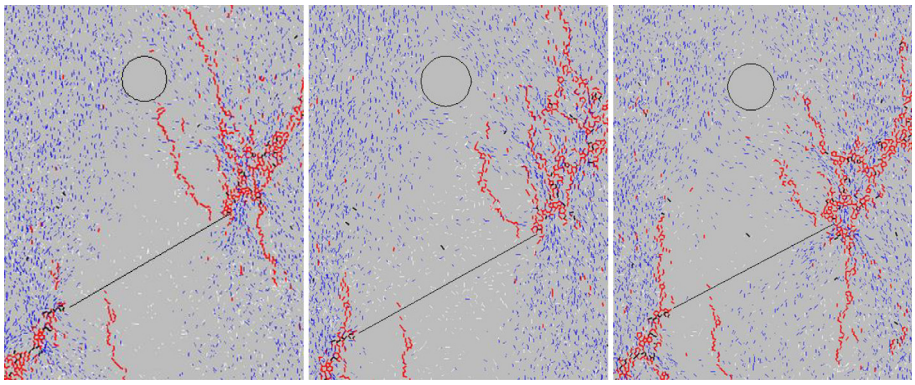

(a) 0.01 m/s (22.8 MPa) (b) 0.08 m/s (23.3 MPa) (c) 0.2 m/s (26.8 MPa)

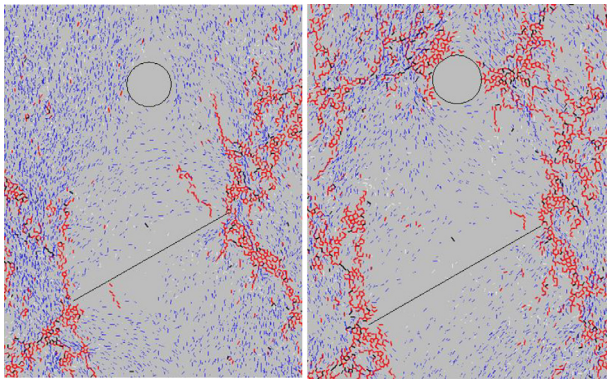

(d) 0.6 m/s (37.8 MPa) (e) 2.0 m/s (71 MPa)

Fig. 4. Stress field of geometry s30-d30 at the peak load at different loading rates.

with previous research (Zhang & Wong, 2013b). As the loading rate increases to 0.2 m/s, the first crack initiation stress increases. When the loading rate increases to 2.0 m/s, the first crack initiation stress is 29 MPa, which is more than twice that at 0.01 m/s. The first crack initiation stress increases with the loading rates, which agrees with the previous experimental research (Zhang & Zhao, 2014). When the loading rate increases, more compressive stress exists between the hole and the pre-existing crack. Compared with Figs. 2(a)–(d), the upper and lower surfaces of the pre-existing crack are compressed, as shown in Fig. 2(e). Meanwhile, the white lines decrease, thus hindering the first crack from propagating.

The stress field when the secondary crack initiates at different loading rates is exhibited in Fig. 3. When the loading rate is 0.01 m/s and the load increases to 19.4 MPa, as shown in Fig. 3(a), more microcracks are initiated near both tips. The white lines in the middle part of the crack become released further. The number of microcracks increases. They connect into macroscopic secondary cracks at the top of the pre-existing crack and develop into a linear band. The first crack connects the hole and the pre-existing crack. The tensile zone around the hole decreases significantly because of the tensile crack. The tensile stress concentration zone below the pre-existing crack propagates further outwards while the compressive zone remains almost the same because the compressive stress can transmit across these microcracks, as shown in Figs. 3(a)–(d). However, in Fig. 3(e), the tensile stress concentration zone below the pre-existing crack does not propagate further because the first crack near the left tip of the pre-existing crack does not appear. As the loading rates increases from 0.01 m/s to 2.0 m/s, the secondary crack initiation stress increases from 19.4 MPa to 29.2 MPa. The loading rate effect is obvious. The space between the hole and the pre-existing crack is free of stress when the loading rate is 0.01 m/s. The first crack does not propagate further when the loading rate is 2.0 m/s, which is caused by the compressive zone between the hole and the pre-existing crack because the first crack is initiated by the tensile stress (Zhou, et al., 2016). Dense blue lines appear around the tips of the pre-existing crack. Hence, the secondary cracks are initiated near the tips of the pre-existing crack. In Figs. 3(d)–(e), the tensile zone around the hole does not

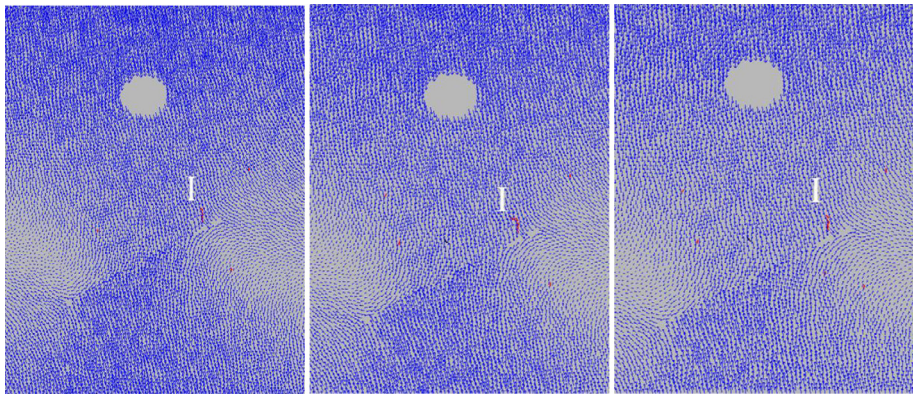

(a) 0.01 m/s (b) 0.08 m/s (c) 0.2 m/s

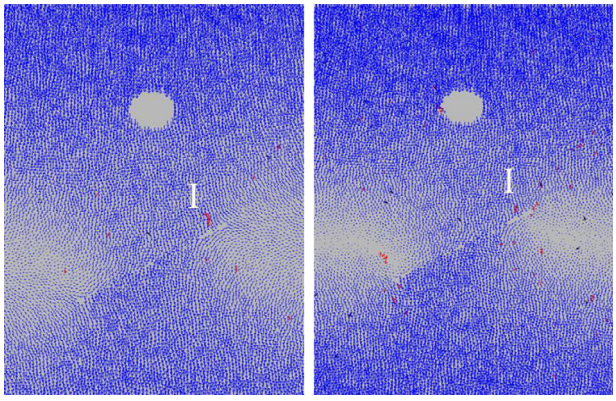

(d) 0.6 m/s (e) 2.0 m/s

Fig. 5. Plots of displacement vectors of geometry s30-d30 when the first crack initiates at different loading rates.

change because no tensile macrocrack exists. The stress in Fig. 3(a) is more uniform than that in Fig. 3(e), which yields more initiated microcracks, as shown in Fig. 3(e). Thus, the local stress concentration in the intact part of the specimen is caused by the high loading rates.

The stress field at the peak load at different loading rates is shown in Fig. 4. When the loading rate is 0.01 m/s and the load increases to 22.8 MPa, as shown in Fig. 4(a), both the compressive stress and the tensile stress between the hole and the crack almost disappear. The hole and the crack become a large defect in the specimen. The same phenomenon occurs at 0.08 m/s. However, when the loading rate increases to 0.6 m/s and 2.0 m/s, the stress still exists between the hole and the pre-existing crack. During the entire compressive test, the compressive stress singularity at both pre-existing crack tips does not disappear, as reported by Bobet (2000) and Zhang & Wong (2013a). The blue lines and the white lines near the left and right sides of the specimen are dense when the loading rate is less than 0.6 m/s. However, they become sparse when the loading rate is 2.0 m/s. This is caused by the initiated cracks in the intact part of the specimen that disturb the stress field. With the loading rates, the compressive strengths also increase, which agrees with previous research (Zou & Wong, 2016).

5 The loading rate effects on the displacement field

The cracking processes also influence the displacement field. The displacement field when the first crack initiates at different loading rates is displayed in Fig. 5. The displacement field types contain type I (relative tensile) and type II (relative tensile and shear) (Carter et al., 1991). The corresponding displacement fields near the crack are marked in the figures. The blue line is the displacement vector and the length of these lines represents the magnitude of displacement in Fig. 5. Before the initiation of the first cracks, the specimen is under compression and the pre-existing crack is almost closed. Subsequently, the microcracks are scattered and unconnected. Most of the particles are still bonded. No significant change in the displacement field is observed. Subsequently, owing to the formation of the macrocrack, the displacement field is disturbed. Macroscopic tensile wing cracks (type-I tensile cracks) are initiated near the tips of the pre-existing crack, which are the first cracks. The displacement field type is associated with type I, as shown in Figs. 5(a)–(e). The macroscopic cracks are expressed as narrow microcracking zones consisting entirely of microscopic tensile cracks. The displacement fields in Figs. 5(a)–(e) do not change significantly. When

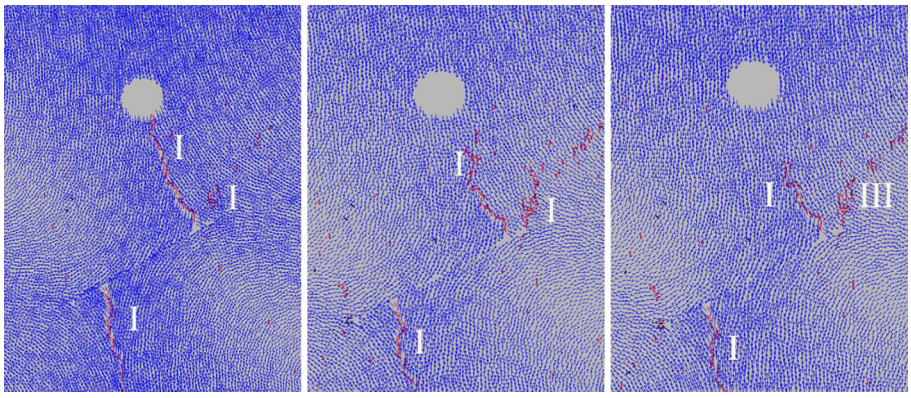

(a) 0.01 m/s (b) 0.08 m/s (c) 0.2 m/s

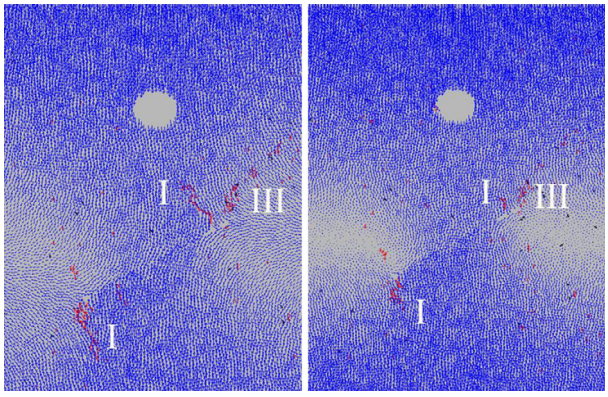

(d) 0.6 m/s (e) 2.0 m/s

Fig. 6. Plots of displacement vectors of geometry s30-d30 when the secondary crack initiates at different loading rates.

(a) Type II displacement field (b) Type III displacement field

Fig. 7. Plots of the moving direction of particles near the crack in type-II and type-III displacement fields.

the loading rates become 0.6 m/s and 2.0 m/s, other microcracks appear. However, they are not connected and are still scattered. Their influence on the displacement field is limited.

The displacement fields when the secondary crack initiates at different loading rates are presented in Fig. 6. In Fig. 6(a), the secondary cracks are activated at the right tip of the pre-existing crack. It is composed of a few tensile microcracks. The tip is associated with the type-I displacement field. However, as the loading rates improve, more shear microcracks appear, as shown in Figs. 6(d)–(e). Compared with previous research (Zhou et al., 2016), a new type of displacement field (i.e., type III) is found, as is shown in Fig. 7(b). The high loading rate leads to the high relative shear velocity between particles, which induces the high shear stress. The moving direction between these two particles is the same. The type-II displacement field at slow loading rates is presented in Fig. 7(a), which is related to the opposite moving direction between particles. From Figs. 6(a)–(e), it can be concluded that the displacement field types depend on the loading rates.

The displacement fields at the peak load at different loading rates are displayed in Fig. 8. The displacement fields change significantly with the loading rates. When the secondary crack occurs, as shown in Fig. 8(a), the displacement field near the first crack is of type I. However, the moving direction of the particles between the hole and the pre-existing crack becomes the same, as shown in Figs. 8(b)–(e). It is related to the type-III displacement field, as shown in Fig. 7(b). A comparison between Figs. 6 and 8 shows that the displacement field types changes with time. When the loading rate is faster than 0.08 m/s, as

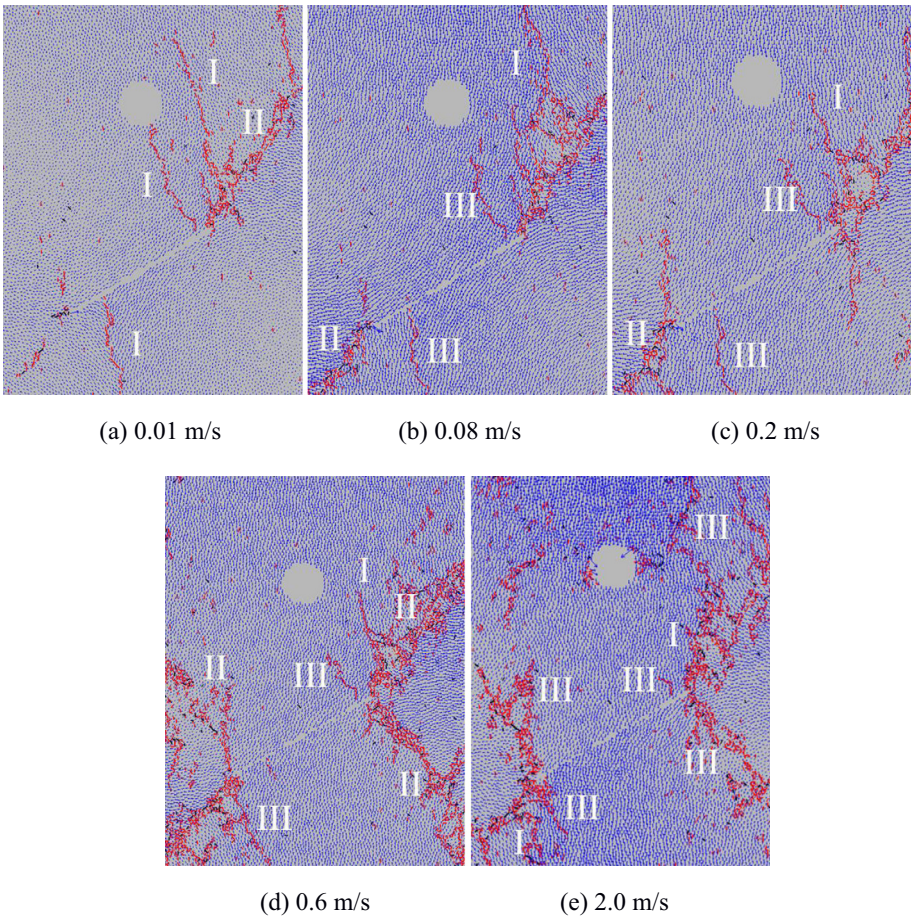

(a) 0.01 m/s (b) 0.08 m/s (c) 0.2 m/s

(d) 0.6 m/s (e) 2.0 m/s

Fig. 8. Plots of displacement vectors of geometry s30-d30 at the peak load at different loading rates.

shown in Figs. 8(b)–(e), the fast loading rate results in different speeds between particles, which yields a broken specimen and a disordered displacement field. The displacement field is influenced by the loading rates. The compressive displacement near the hole in Fig. 8(e) is larger than that in Figs. 8(a)–(d). The shielding effect of the hole becomes more obvious. No coalescence crack occurs, as shown in Figs. 8(b)–(e). Hence, the hole is easier to be broken by compression at higher loading rates while it tends to be broken by the coalescence crack at lower loading rates.

6 Conclusions

We studied the cracking processes of rock-like specimens containing a circular hole and a pre-existing crack at different loading rates using the DEM approach. The similarities and differences in the displacement field and stress field at different loading rates were investigated. Based on the investigation, the following conclusions are drawn.

The loading rates influenced the primary and secondary cracks, which disturbed the stress field and displacement field. The rate-dependence was weak below 0.08 m/s, and became significant when the loading rates increased to 2.0 m/s. A relatively larger amount of microcracks were initiated at different positions of the specimens at high loading rates owing to the local stress concentration, while only a few initiated around the flaw at slow loading rates. The displacement field types depended on the loading rates and a new displacement field type was observed. The evolutions of the displacement field and stress field at different loading rates were analyzed. The hole was easier to be broken by compression at higher loading rates owing to the stress concentration, while it was more likely to be broken by the coalescence crack at lower loading rates. The high loading rates caused the shielding effects of the hole on the pre-existing crack and no coalescence crack occurred.

Acknowledgements

This work was supported by the Sofa-Kovalevskaja Award of Alexander von Humboldt Foundation.

References

Amiri, F., Milan, D., Shen, Y., Rabczuk, T., & Arroyo, M. (2014). Phase-field modeling of fracture in linear thin shells. *Theoretical and Applied Fracture Mechanics, 69*, 102–109.

Amiri, F., Anitescu, C., Arroyo, M., Bordas, S., & Rabczuk, T. (2014). XLME interpolants, a seamless bridge between XFEM and enriched meshless methods. *Computational Mechanics, 53*(1), 45–57.

Areias, P., Rabczuk, T., & Msekh, M. A. (2016). Phase-field analysis of finite-strain plates and shells including element subdivision. *Computer Methods in Applied Mechanics and Engineering, 312*, 322–350.

Badnava, H., Msekh, M. A., Etemadi, E., & Rabczuk, T. (2018). An h-adaptive thermo-mechanical phase field model for fracture. *Finite Elements in Analysis and Design, 138*, 31–47.

Bek, Y. K., Hamdia, K. M., Rabczuk, T., & Könke, C. (2018). Micromechanical model for polymeric nano-composites material based on SBFEM. *Composite Structures*. doi:10.1016/j.compstruct.2018.03.064.

Bobet, A. (2000). The initiation of secondary cracks in compression. *Engineering Fracture Mechanics, 66*(2), 187–219.

Carter, B. J., Lajtai, E. Z., & Petukhov, A. (1991). Primary and remote fracture around underground cavities. *International Journal for Numerical and Analytical Methods in Geomechanics, 15*(1), 21–40.

Chau-Dinh, T., Zi, G., Lee, P. S., Rabczuk, T., & Song, J. H. (2012). Phantom-node method for shell models with arbitrary cracks. *Computers & Structures, 92*, 242–256.

Chen, L., Rabczuk, T., Bordas, S. P. A., Liu, G. R., Zeng, K. Y., & Kerfriden, P. (2012). Extended finite element method with edge-based strain smoothing (ESm-XFEM) for linear elastic crack growth. *Computer Methods in Applied Mechanics and Engineering, 209*, 250–265.

Dai, F., Xia, K., Zheng, H., & Wang, Y. X. (2011). Determination of dynamic rock mode-I fracture parameters using cracked chevron notched semi-circular bend specimen. *Engineering Fracture Mechanics, 78*(15), 2633–2644.

Ghazvinian, A., Sarfarazi, V., Schubert, W., & Blumel, M. (2012). A study of the failure mechanism of planar non-persistent open joints using PFC2D. *Rock Mechanics and Rock Engineering, 45*(5), 677–693.

Ghorashi, S., Valizadeh, N., Mohammadi, S., & Rabczuk, T. (2015). T-spline based XIGA for fracture analysis of orthotropic media. *Computers & Structures, 147*, 138–146.

Hamdia, K. M., Silani, M., Zhuang, X., He, P., & Rabczuk, T. (2017). Stochastic analysis of the fracture toughness of polymeric nanoparticle composites using polynomial chaos expansions. *International Journal of Fracture, 206*(2), 215–227.

Itasca (2004). PFC2D (Particle Flow Code in 2 Dimensions) Version 3.1. Minneapolis.

Jackson, K., Kingman, S. W., Whittles, D. N., Lowndes, I. S., & Reddish, D. J. (2008). The effect of strain rate on the breakage behaviour of rock. *Archives of Mining Sciences, 53*(1), 3–22.

Kranz, R. L. (1979). Crack-crack and crack-pore interactions in stressed granite. *International Journal of Rock Mechanics and Mining Sciences, 16*(1), 37–47.

Lee, H., & Jeon, S. (2011). An experimental and numerical study of fracture coalescence in pre-cracked specimens under uniaxial compression. *International Journal of Solids and Structures, 48*(6), 979–999.

Lee, H. K., & Ju, J. W. (2007). A three-dimensional stress analysis of a penny-shaped crack interacting with a spherical inclusion. *International Journal of Damage Mechanics, 16*(3), 331–359.

Ma, T., Zhang, Y., Zhang, D., Yan, J., & Ye, Q. (2016). Influences by air voids on fatigue life of asphalt mixture based on discrete element method. *Construction and Building Materials, 126*, 785–799.

Msekh, M. A., Cuong, N. H., Zi, G., Areias, P., Zhuang, X., & Rabczuk, T. (2017). Fracture properties prediction of clay/epoxy nanocomposites with interphase zones using a phase field model. *Engineering Fracture Mechanics, 188*, 287–299.

Nguyen-Thanh, N., Valizadeh, N., Nguyen, M. N., Nguyen-Xuan, H., Zhuang, X., Areias, P., ... Rabczuk, T. (2015). An extended isogeometric thin shell analysis based on Kirchhoff-Love theory. *Computer Methods in Applied Mechanics and Engineering, 284*, 265–291.

Nguyen-Xuan, H., Liu, G. R., Bordas, S., Natarajan, S., & Rabczuk, T. (2013). An adaptive singular ES-FEM for mechanics problems with singular field of arbitrary order. *Computer Methods in Applied Mechanics and Engineering, 253*, 252–273.

Olsson, W. A. (1991). The compressive strength of tuff as a function of strain rate from 10^{-6} to 10^{3}/sec. *International Journal of Rock Mechanics and Mining Sciences, 28*(1), 115–118.

Perras, M. A., & Diederichs, M. S. (2014). A review of the tensile strength of rock: Concepts and testing. *Geotechnical and Geological Engineering, 32*(2), 525–546.

Potyondy, D. O., & Cundall, P. A. (2004). A bonded-particle model for rock. *International Journal of Rock Mechanics and Mining Sciences, 41*(8), 1329–1364.

Rabczuk, T., Areias, P., & Belytschko, T. (2007). A meshfree thin shell method for non-linear dynamic fracture. *International Journal for Numerical Methods in Engineering, 72*(5), 524–548.

Rabczuk, T., & Belytschko, T. (2004). Cracking particles: A simplified meshfree method for arbitrary evolving cracks. *International Journal for Numerical Methods in Engineering, 61*(13), 2316–2343.

Rabczuk, T., Gracie, R., Song, J. H., & Belytschko, T. (2010). Immersed particle method for fluid-structure interaction. *International Journal for Numerical Methods in Engineering, 81*(1), 48–71.

Ren, H., Zhuang, X., Cai, Y., & Rabczuk, T. (2016). Dual-Horizon peridynamics. *International Journal for Numerical Methods in Engineering, 108*(12), 1451–1476.

Ren, H., Zhuang, X., & Rabczuk, T. (2017). Dual-horizon peridynamics: A stable solution to varying horizons. *Computer Methods in Applied Mechanics and Engineering, 318*, 762–782.

Wong, L. N. Y., & Einstein, H. H. (2009a). Crack coalescence in molded gypsum and Carrara marble: Part 1. Macroscopic observations and interpretation. *Rock Mechanics and Rock Engineering, 42*(3), 475–511.

Wong, L. N. Y., & Einstein, H. H. (2009b). Systematic evaluation of cracking behavior in specimens containing single flaws under uniaxial compression. *International Journal of Rock Mechanics and Mining Sciences, 46*(2), 239–249.

Xie, B., Guo, J. J., & Xia, X. (2012). Influence of loading rate on uniaxial compression test of rock specimen with random joints. *Advanced Materials Research, 396*, 217–220.

Zhang, Q. B., & Zhao, J. (2013). Effect of loading rate on fracture toughness and failure micromechanisms in marble. *Engineering Fracture Mechanics, 102*, 288–309.

Zhang, Q. B., & Zhao, J. (2014). Quasi-static and dynamic fracture behaviour of rock materials: Phenomena and mechanisms. *International Journal of Fracture, 189*(1), 1–32.

Zhang, X. P., & Wong, L. N. Y. (2012). Cracking processes in rock-like material containing a single flaw under uniaxial compression: A numerical study based on parallel bonded-particle model approach. *Rock Mechanics and Rock Engineering, 45*(5), 711–737.

Zhang, X. P., & Wong, L. N. Y. (2013a). Crack initiation, propagation and coalescence in rock-like material containing two flaws: A numerical study based on bonded-particle model approach. *Rock Mechanics and Rock Engineering, 46*(5), 1001–1021.

Zhang, X. P., & Wong, L. N. Y. (2013b). Loading rate effects on cracking behavior of flaw-contained specimens under uniaxial compression. *International Journal of Fracture, 180*(1), 93–110.

Zhou, S., Zhu, H., Ju, J. W., Yan, Z., & Chen, Q. (2017). Modeling microcapsule-enabled self-healing cementitious composite materials using discrete element method. *International Journal of Damage Mechanics, 26*(2), 340–357.

Zhou, S., Zhu, H., Yan, Z., Ju, J. W., & Zhang, L. (2016). A micromechanical study of the breakage mechanism of microcapsules in concrete using PFC2D. *Construction and Building Materials, 115*, 452–463.

Zhuang, X., Cai, Y., & Augarde, C. (2014). A meshless sub-region radial point interpolation method for accurate calculation of crack tip fields. *Theoretical and Applied Fracture Mechanics, 69*, 118–125.

Zhuang, X., Zhu, H., & Augarde, C. (2014). An improved meshless Shepard and least squares method possessing the delta property and requiring no singular weight function. *Computational Mechanics, 53*(2), 343–357.

Zhuang, X., & Zhou, S. (2018). Molecular dynamics study of an amorphous polyethylene/silica interface with shear tests. *Materials, 11*(6), 929.

Zou, C., & Wong, L. N. Y. (2016). Different compressive and tensile strength of moulded gypsum under various strain rates from quasi-static to dynamic regime. *Geotechnical Testing Journal, 39*(4), 596–607.